Lawrence Berkeley National Laboratory

Title

Tracing intermolecular Coulombic decay of carbon-dioxide dimers and oxygen dimers after valence photoionization

Authors

Iskandar, W
Gatton, AS
Gaire, B
et al.

Tracing intermolecular Coulombic decay of carbon-dioxide dimers and oxygen dimers after valence photoionization

W. Iskandar,[1,*] A. S. Gatton,[1] B. Gaire,[1] F. P. Sturm,[1] K. A. Larsen,[1,2] E. G. Champenois,[1,2] N. Shivaram,[1]
A. Moradmand,[3] J. B. Williams,[4] B. Berry,[5] T. Severt,[5] I. Ben-Itzhak,[5] D. Metz,[6] H. Sann,[6] M. Weller,[6]
M. Schoeffler,[6] T. Jahnke,[6] R. Dörner,[6] D. Slaughter,[1] and Th. Weber[1,†]

[1]*Chemical Sciences Division, Lawrence Berkeley National Laboratory, Berkeley, California 94720, USA*
[2]*Graduate Group in Applied Science and Technology, University of California, Berkeley, California 94720, USA*
[3]*Department of Physics, Auburn University, Auburn, Alabama 36849, USA*
[4]*Department of Physics, University of Nevada, Reno, Nevada 89557, USA*
[5]*J. R. Macdonald Laboratory, Department of Physics, Kansas State University, Manhattan, Kansas 66506, USA*
[6]*Institut für Kernphysik, Goethe-Universitaet, Max-von-Laue-Strasse 1, D-60438 Frankfurt am Main, Germany*

We have conducted an experimental study on the photo double ionization (PDI) of carbon-dioxide dimers at photon energies of 37 and 55 eV and oxygen dimers at photon energies of 38, 41.5, and 46 eV, while focusing on the dissociation dynamics upon single-photon absorption. The investigation was performed by applying the cold-target recoil-ion momentum spectroscopy method in order to collect and record the three-dimensional momenta of the ionic fragments and emitted electrons from the dissociating dimer in coincidence. The kinetic-energy release upon fragmentation and the electron angular distributions in the laboratory and body-fixed frames, as well as the relative electron-electron emission angle, show unambiguous experimental evidence of intermolecular Coulombic decay (ICD) in carbon-dioxide dimers upon photoionization below and above the double-ionization threshold of CO_2 monomers. The PDI of oxygen dimers is less conclusive and shows contributions from ICD and knock-off ionization mechanisms. As for atomic dimers, the present results reveal that ICD in CO_2 dimers after valence PDI can also serve as a source for low-energy electrons, known to be very relevant in biological systems, cells, and tissues.

I. INTRODUCTION

In the last two decades, interatomic (or intermolecular) Coulombic decay (ICD) was found to be a very common relaxation pathway in nature that occurs after exciting a weakly bound system (e.g., in van der Waals or hydrogen bonds) by ion, electron, or photon impact [1–6] (see, e.g., [7,8] for recent reviews on the topic). This process occurs when an excited system embedded in an environment, such as a loosely bound neighboring atom or molecule, relaxes by transferring the excess excitation energy to the neighboring atom or molecule causing its ionization. This energy release typically happens on a femtosecond timescale and leads to the removal of a low-energy secondary electron from the neighboring site of the order of few electron volts. The cations, formed as a result of the decay, repel each other and initiate a Coulomb explosion of the system.

ICD was first theoretically predicted for hydrogen-bonded systems and van der Waals clusters of noble-gas atoms [9–11]. A few years later, experimental evidence of ICD was reported in neon clusters [1,12,13] and, later, in other noble-gas dimers (e.g., He_2, Ar_2, and ArNe) [14–17]. The investigations of the past decade demonstrated that ICD can be very efficient

and proceeds within significantly less than 100 femtoseconds in some systems [13], quenching other energetically allowed but slower relaxation processes of the excited dimer, e.g., fluorescence emissions that occur on picosecond timescales. Along with atomic clusters, a few studies were also performed on molecular clusters that comprise van der Waals bonds (N_2 and CO dimers) [18] or hydrogen bonds (e.g., water clusters and aqueous solutions) [2,19,20]. In the aforementioned work on van der Waals bound molecules, ICD has been triggered by a resonant Auger decay after core excitation [18]. However, ICD after direct inner-valence ionization of molecular clusters remains, so far, widely unexplored.

Studying ICD processes is very valuable for our understanding of fundamental ionization mechanisms in photochemistry and is of multidisciplinary relevance especially in weakly bound matter, e.g., biological systems. This is because the ejected low-energy electrons accompanying the ICD process are prone to induce biological damage such as DNA strand breaks. Moreover, the radical cationic fragments can react with the surrounding biomolecules, causing further damage to the biological system in secondary reactions [21,22]. On the positive side, ICD is expected to play an important role as a repair mechanism for DNA enzymes [23].

Many challenges arise in terms of a clean detection and interpretation of ICD in the photoionization of molecular dimers. Many other ultrafast relaxation processes compete with ICD, including (resonant) charge transfer, electron

*wiskandar@lbl.gov
†tweber@lbl.gov

transfer mediated decays [24], or even direct photo-double-ionization (PDI) processes along the knock-off two-step-one (TS1) scheme [25]. In atomic clusters, these different contributions to the double ionization of a dimer target can be disentangled in most cases by investigating the coincidence maps of ion and electron kinetic energies. The higher structural complexity of molecular clusters, however, demands that geometry-dependent photoelectron binding energies, a higher number of initial and final electronic states, and vibrational and rotational degrees of freedom of the ionic fragments be taken into account. Therefore, ICD energy spectra of molecular dimers are much broader and less structured than those of rare-gas atomic systems, making it much harder to unambiguously identify the ICD process. Nevertheless, past studies on molecular systems revealed ICD to be a prominent decay channel, occurring on timescales that are even shorter than those of most noble-gas systems [18]. This ultrashort decay time is expected to be a general feature of ICD in molecular systems, as the decay needs to outpace a possible dissociation of the molecule that was initially excited by either photon absorption or particle impact.

The present work is devoted to the investigation of radiation damage to carbon-dioxide dimers and oxygen dimers by single photons. In particular, we investigate the dissociation pathways of the CO_2 dimer upon PDI below and above the double-ionization threshold of the CO_2 monomer. We compare these findings with dissociative PDI of O_2 dimers for three different photon energies above the PDI threshold of O_2 monomers. For isolated molecules, the pathways leading to ejection of two electrons and a subsequent ionic fragmentation are direct photodissociation, predissociation, or autoionization. For molecular dimers, these processes ionize only one site of the dimer directly, leaving the second site intact, unless a secondary reaction such as ICD, charge transfer, or a two-site electron knock-off process is triggered. In this work, we investigate the competition between one-site and two-site ionization of the molecular dimer systems. Our studies focus on the symmetric $CO_2^+ + CO_2^+$ and $O_2^+ + O_2^+$ dimer fragmentation channels. This is technically challenging as the target density in a gas jet amounts to typically only one to three percent of the available monomers and the cross section for PDI is expected to be a factor of 10 to 100 lower than the single photoionization of the target. Therefore, collecting statistically significant datasets, sufficient for highly differential analysis, of these rare events is highly challenging. However, with modern spectroscopic technologies such as reaction microscopy [26–28], the different competing ionization mechanisms and dissociation dynamics can be resolved in highly differential spectra of few-body breakups of rather simple systems, as demonstrated in this work. We show that ICD in CO_2 dimers unambiguously takes place and is the dominating dissociation mechanism. In the O_2 dimer, which is comparable with the CO_2 dimer in terms of structure and number of states, ICD is accompanied by direct PDI. We use the measured kinetic energies of the emitted electrons, the body-fixed frame electron angular distributions, as well as the kinetic-energy release (KER) of the cations as observables to identify the electronic states involved and the decay processes taking place after irradiating the dimer target with XUV photons.

II. EXPERIMENTAL SETUP

The experiments were performed at beam line 10.0.1.3 at the Advanced Light Source in Berkeley using 37.0 and 55.0 eV photons to investigate the fragmentation dynamics of CO_2 dimer targets and 38.0, 41.5, and 46.0 eV photons for the PDI of O_2 dimer targets. The photon-energy resolution was set to approximately 50 meV using the 10.0.1 monochromator [29]. The dimers were produced by adiabatically expanding the pure target gas through a 50 μm nozzle at room temperature and at a stagnation pressure of 0.5 bar for CO_2 and 10 bar for O_2 gas. The supersonic beam was collimated laterally by a set of two skimmers and then crossed with the photon beam inside a reaction microscope, also known as cold-target recoil-ion momentum spectroscopy (COLTRIMS) apparatus [26–28]. A static electric field (11.45 V/cm for the CO_2 experiment and 6.05 V/cm for the O_2 experiment) and a parallel magnetic field (9.95 G for the CO_2 and 7.21 G for the O_2 experiment) guided electrons and ions to two microchannel plate detectors equipped with delay line readout [30,31], which were located at the opposite ends of the spectrometer. The extraction and guiding fields were adjusted such that electrons of up to 26 and 17 eV for the CO_2 and O_2 experiments, respectively, could be collected with a 4π solid angle. With these configurations, ionic CO_2^+ fragments of up to 15 eV kinetic energy and O_2^+ fragments of up to 8 eV kinetic energy could be detected independent of their initial emission direction. The time of flight (TOF) and position of impact of two ionic fragments and two electrons were detected in coincidence and processed by offline analysis. The datasets were reduced to coincidence events containing two cations (CO_2^+ or O_2^+) plus two electrons from each of the dimer targets via placing software restrictions on the photoion-photoion coincidence (PIPICO) TOF spectra and electron-ion energy correlation diagrams. The three-dimensional (3D) momentum vectors of the ions and electrons were calculated using the recorded positions of impact and TOFs of the respective particles. For double-ionization mechanisms such as knock-off or ICD, the timescales are ultrafast and, as a consequence, the resulting Coulomb explosion occurs with little to no delay after the electrons are emitted. We therefore expect no rotation of the recoil axis of the ionic breakup and assume the axial recoil approximation [32,33] to be valid. A check on momentum conservation for the recoil-ionic fragments was used to reject false coincidences. The kinetic-energy release (KER) of the ionic fragments and the orientation of the dimer axis at the moment of photodissociation were then inferred from the 3D momenta of the fragment ions in the dimer center-of-mass frame. The measured laboratory frame electron momenta were used to generate angular distributions with respect to the linear polarization vector of the XUV light. Moreover, they were transferred into the body-fixed frame to generate so-called recoil frame photoelectron angular distributions (RFPADs).

Along with the $CO_2^+ + CO_2^+$ dimer breakup channel, our detection system also collects the $CO^+ + O^+$ monomer fragmentation channel. The same restrictions and analysis procedure as described above is applied to this channel, and its yield is compared to the number of events of the $CO_2^+ + CO_2^+$ fragmentation channel. For instance, for 55 eV
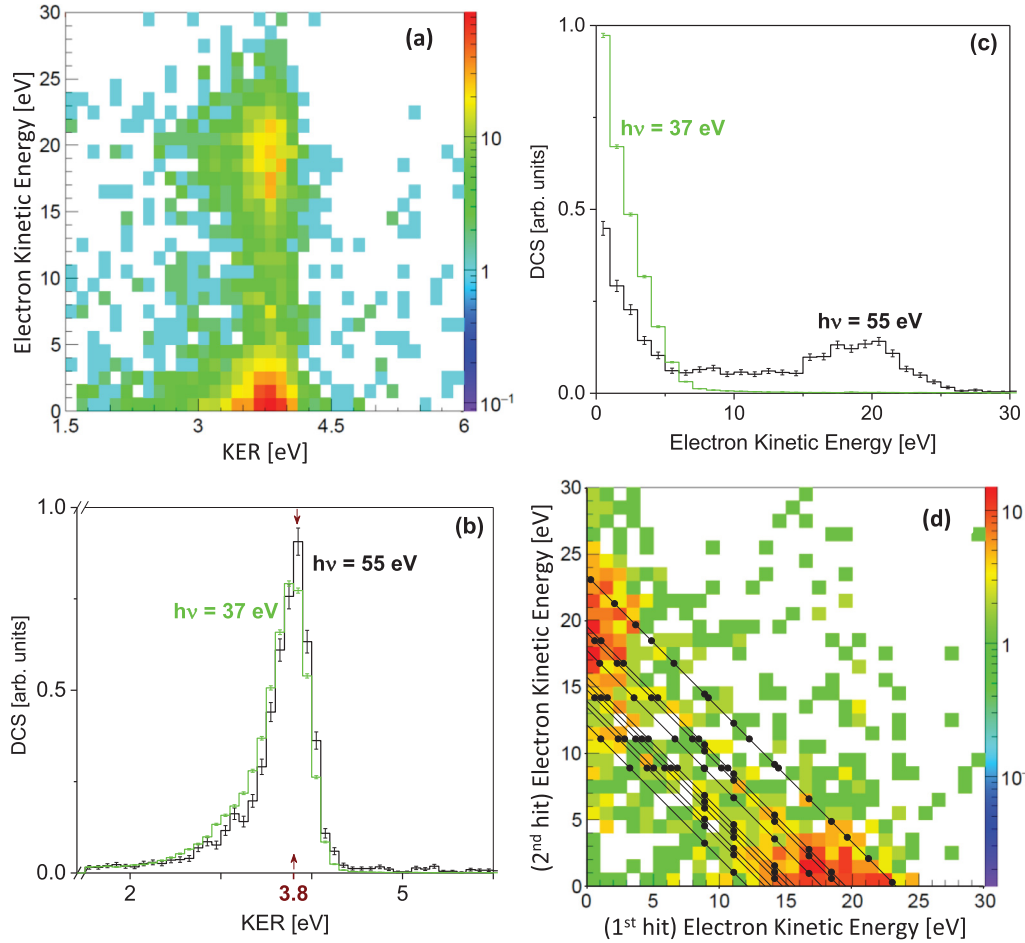
FIG. 1. (a) Yield of the $CO_2^+ + CO_2^+$ dimer breakup at 55 eV photon energy as a function of the kinetic-energy release (KER) and the kinetic energy of either emitted electrons. (b) Differential cross section (DCS) in KER distributions for the $CO_2^+ + CO_2^+$ fragmentation channel at photon energies of 37 eV [green (gray) line] and 55 eV (black line), showing the same shape and a maximum located at 3.8 eV. (c) Differential cross section (DCS) in electron energy distribution of the PDI of CO_2 dimers for a photon energy of 55 eV (black line), showing two distinct contributions from the low-energy and high-energy electrons featuring the ICD process and for a photon energy of 37 eV [green (gray) line]. (d) Electron energy correlation map showing the yield of the $CO_2^+ + CO_2^+$ dimer breakup as a function of the energy of the first and the second detected electron for a photon energy of 55 eV. The estimated energy maps of the emitted electrons for direct PDI (diagonal black lines) and ICD (black dots) processes, taken from Tables II and III for a photon energy of 55 eV, are overlaid in order to identify the states involved and their yields. The yields in (a) and (d) are given on a logarithmic color scale.

photons, the $CO_2^+ + CO_2^+$ dimer breakup amounts to only 1.5% relative to the observed double-ionization yield of the monomer, i.e., the $CO^+ + O^+$ fragmentation channel. The small percentage of 1.5 reflects the low dimer fraction in the CO_2 supersonic gas jet. For the $O_2^+ + O_2^+$ dimer breakup channel, we find a value of 1% with respect to the $O^+ + O^+$ monomer fragmentation channel.

III. RESULTS

A. Kinetic energy of fragment ions and electrons

1. $CO_2^+ + CO_2^+$ fragmentation channel
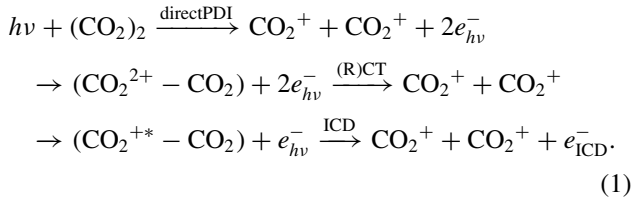
In Fig. 1(a), we plot the yield of the $CO_2^+ + CO_2^+$ dimer breakup at 55 eV photon energy as a function of KER and the kinetic energy of either emitted electrons, as an example for qualitatively probing the potential-energy surface of the dimer dication. We identify two islands, which relate the

measured KER distribution around 3.8 eV with a fast electron at about 19 eV and a coincident slow electron with about 1 eV. Observing two emitted electrons with very different kinetic energies indicates that a sequential ionization mechanism is preferentially taking place at that photon energy. In the next step, we relate these energies more quantitatively to each other and identify the electronic states at play. We realize this by projecting the electron-ion energy correlation map to the respective axes in Figs. 1(b) and 1(c) and investigate the KER distribution and the kinetic electron energies in more detail below.

The KER distributions obtained for the $CO_2^+ + CO_2^+$ fragmentation channel are displayed in Fig. 1(b) for photon energies of 37 eV (green line) and 55 eV (black line). Both distributions show the same shape, meaning that similar dissociation processes are involved for the two photon energies. For both photon energies, the KER peaks at 3.8 eV. The KER can be converted to an internuclear separation of 7.15 a.u.

between the two CO_2^+ ions at the instant of photodissociation assuming a $1/R$ potential between the two singly charged fragments, approximated as point charges, that repel each other. This value is very close to the equilibrium internuclear distance of the most stable geometry of CO_2 dimers, which is the slipped parallel $/-/$ $(60; 60; 0)$ configuration, located around 6.7 a.u. [34].

As seen in previous double-ionization studies for an atomic dimer [4,16,24,25], the fragmentation into the $CO_2^+ + CO_2^+$ channel can result not only from a one-site single-ionization and excitation process followed by ICD, but also from two competing double-ionization processes: a two-site double ionization called the direct PDI process, wherein one electron is removed from each molecule of the dimer, leading directly to a Coulomb explosion, or a one-site double ionization populating $CO_2^{2+} - CO_2$ nondissociative molecular states. The latter transient states relax in a second step through radiative charge transfer (RCT), i.e., charge transfer accompanied by emission of a photon(s), or via charge transfer (CT) at direct crossings to the same dissociative states as the two-site double-ionization $CO_2^+ + CO_2^+$ events. The three reactions are described as follows:

$$h\nu + (CO_2)_2 \xrightarrow{\text{directPDI}} CO_2^+ + CO_2^+ + 2e_{h\nu}^-$$
$$\rightarrow (CO_2^{2+} - CO_2) + 2e_{h\nu}^- \xrightarrow{\text{(R)CT}} CO_2^+ + CO_2^+$$
$$\rightarrow (CO_2^{+*} - CO_2) + e_{h\nu}^- \xrightarrow{\text{ICD}} CO_2^+ + CO_2^+ + e_{\text{ICD}}^-.$$
$$(1)$$

In order to identify which of these dissociation pathways is at play for the detected $CO_2^+ + CO_2^+$ breakup channel, the electronic structure of the relevant states (see Table I) of the cation and dication of an isolated CO_2 molecule have to be considered. Here we have used the electron momentum spectroscopy measurements of Tian *et al.* [35] for the outer- and inner-valence states of the carbon-dioxide singly charged ion, the calculations of Millie *et al.* [36], and the measurements of Slattery *et al.* [37] for the assignments of the metastable doubly charged CO_2^{2+} states. The electron configuration of the occupied outer-valence (OV) and inner-valence (IV) orbitals of CO_2 is $[4\sigma_g^2 3\sigma_u^2 1\pi_u^4 1\pi_g^4]$ and $[3\sigma_g^2 2\sigma_u^2]$, respectively. The removal of one electron from one of the four highest orbitals of the molecule leads to the outer-valence electronic states of the CO_2^+ cation $X\,^2\Pi_g$, $A\,^2\Pi_u$, $B\,^2\Sigma_u^+$, or $C\,^2\Sigma_g^+$. These four states are nondissociative, except for the high vibrational levels of the $C\,^2\Sigma_g^+$ state, which lead to a dissociation of the CO_2^+ molecular ion into $CO^+ + O$ or $CO + O^+$ fragments. For the $CO_2^+ + CO_2^+$ fragmentation channel under investigation, we only consider these four outer-valence electronic states of the CO_2^+ cation in the final ionic products. For the ICD process, we consider the inner-valence electronic $^2\Sigma_u^+$ and $^2\Sigma_g^+$ satellite states of the excited CO_2^{+*} cation. The potential-energy curves of these excited molecular states, like those having an inner-valence vacancy, are steeply repulsive along the asymmetric C-O coordinate. Therefore, if ICD takes place, it needs to happen fast enough in order to compete with the one-site dissociative processes. Such competing processes are direct dissociation of the CO_2^{+*} site of the dimer into $CO^+ + O$ or $CO + O^+$ or autoionization into $CO^+ + O^+$.

TABLE I. Molecular states and vertical ionization potentials (VIPs) of a neutral, singly, and doubly charged CO_2 molecule [35–37]. Note the electronic configuration of the CO_2 molecule: $[3\sigma_g^2 2\sigma_u^2]_{\text{IV}}$ $[4\sigma_g^2 3\sigma_u^2 1\pi_u^4 1\pi_g^4]_{\text{OV}}$, where IV stands for inner-valence orbital and OV stands for outer-valence orbital.

Species	State	VIP (eV)
CO_2	$X\,^1\Pi_g$	0.0
$CO_2^+{}_{\text{OV}}$	$X\,^2\Pi_g\,[1\pi_g^{-1}]$	13.78
	$A\,^2\Pi_u\,[1\pi_u^{-1}]$	17.60
	$B\,^2\Sigma_u^+\,[3\sigma_u^{-1}]$	18.08
	$C\,^2\Sigma_g^+\,[4\sigma_g^{-1}]$	19.40
$CO_2^{+*}{}_{\text{IV}}$	$^2\Sigma_u^+\,[2\sigma_u^{-1}]$	31.9
		33.7
		35.3
	$^2\Sigma_g^+\,[3\sigma_g^{-1}]$	36.5
		38.2
		40.8
		43.9
		46.1
CO_2^{2+}	$X\,^3\Sigma_g^-\,[1\pi_g^{-2}]$	37.34
	$a\,^1\Delta_g\,[1\pi_g^{-2}]$	38.52
	$b\,^1\Sigma_g^+\,[1\pi_g^{-2}]$	39.16
	$c\,^1\Sigma_u^-\,[1\pi_u^{-1}1\pi_g^{-1}]$	40.10
	$A\,^3\Delta_u\,[1\pi_u^{-1}1\pi_g^{-1}]$	40.59
	$B\,^3\Sigma_u^-\,[1\pi_u^{-1}1\pi_g^{-1}]$	40.78
	$D\,^3\Pi_u\,[3\sigma_u^{-1}1\pi_g^{-1}]$	41.43
	$C\,^3\Sigma_u^-\,[1\pi_u^{-1}1\pi_g^{-1}]$	42.19
	$d\,^1\Pi_u\,[3\sigma_u^{-1}1\pi_g^{-1}]$	42.30
	$E\,^3\Pi_g\,[4\sigma_g^{-1}1\pi_g^{-1}]$	42.65
	$e\,^1\Pi_g\,[4\sigma_g^{-1}1\pi_g^{-1}]$	42.82

For the RCT and CT processes, the lowest electronic states of the CO_2^{2+} dication are listed in Table I. In a single electron transition from the $1\pi_g$ orbital of the neutral CO_2 to CO_2^{2+}, the ground state $X\,^2\Pi_g$ of the product CO_2^+ can be formed from all listed reactant states of CO_2^{2+}. Similar considerations can be applied to $1\pi_u$, $3\sigma_u$, and $4\sigma_g$ orbitals of the neutral CO_2. The CO_2^+ $A\,^2\Pi_u$ state can be produced from the CO_2^{2+} states $c\,^1\Sigma_u^-$, $A\,^3\Delta_u$, $B\,^3\Sigma_u^-$, and $C\,^3\Sigma_u^-$, the CO_2^+ $B\,^2\Sigma_u^+$ state can be produced from CO_2^{2+} states $D\,^3\Pi_u$ and $d\,^1\Pi_u$, and the CO_2^+ $C\,^2\Sigma_g^+$ state can be produced from CO_2^{2+} states $E\,^3\Pi_g$ and $e\,^1\Pi_g$. In addition to these transitions, other weaker transitions may happen, involving electron transfer driven by spin-orbit coupling; however, those are not taken into account in the present analysis.

Based on this information and Table I, we estimate the kinetic energy of the emitted electrons for each process. We then compare these values to the experimental data presented in Figs. 1(c) and 1(d). For the direct PDI and (radiative) charge transfer processes, the energy sharing $E_s = KE(e_1)/[KE(e_1) + KE(e_2)]$ between the two emitted electrons e_1 and e_2 is uniform and only their energy sum $KE(e_1) + KE(e_2)$ is estimated and presented in Table II. By taking into account the four bound states [X, A, B, and C] of the

TABLE II. Molecular states of each site of the dimer, vertical ionization potentials (VIPs), estimated from potential-energy curves at the equilibrium distance of the dimer (6.7 a.u.), and electron energy sum for photon energies of 37 and 55 eV.

States	VIP (eV)	Electron Energy Sum (eV)	
		$h\nu = 37$ eV	$h\nu = 55$ eV
$CO_2^+ - CO_2^+$		Direct PDI	Direct PDI
$X\,^2\Pi_g$-$X\,^2\Pi_g$	31.62	5.38	23.38
$X\,^2\Pi_g$-$A\,^2\Pi_u$	35.44	1.56	19.56
$X\,^2\Pi_g$-$B\,^2\Sigma_u^+$	35.92	1.08	19.08
$X\,^2\Pi_g$-$C\,^2\Sigma_g^+$	37.24		17.76
$A\,^2\Pi_u$-$A\,^2\Pi_u$	39.26		15.74
$A\,^2\Pi_u$-$B\,^2\Sigma_u^+$	39.74		15.26
$A\,^2\Pi_u$-$C\,^2\Sigma_g^+$	41.06		13.94
$B\,^2\Sigma_u^+$-$B\,^2\Sigma_u^+$	40.22		14.78
$B\,^2\Sigma_u^+$-$C\,^2\Sigma_g^+$	41.54		13.46
$C\,^2\Sigma_g^+$-$C\,^2\Sigma_g^+$	42.86		12.14
$CO_2^{2+} - CO_2$			RCT and CT
$X\,^3\Sigma_g^-$-$X\,^1\Pi_g$	37.34		17.66
$a\,^1\Delta_g$-$X\,^1\Pi_g$	38.52		16.48
$b\,^1\Sigma_g^+$-$X\,^1\Pi_g$	39.16		15.84
$c\,^1\Sigma_u^-$-$X\,^1\Pi_g$	40.10		14.9
$A\,^3\Delta_u$-$X\,^1\Pi_g$	40.59		14.41
$B\,^3\Sigma_u^-$-$X\,^1\Pi_g$	40.78		14.22
$D\,^3\Pi_u$-$X\,^1\Pi_g$	41.43		13.57
$C\,^3\Sigma_u^-$-$X\,^1\Pi_g$	42.19		12.81
$d\,^1\Pi_u$-$X\,^1\Pi_g$	42.30		12.7
$E\,^3\Pi_g$-$X\,^1\Pi_g$	42.65		12.35
$e\,^1\Pi_g$-$X\,^1\Pi_g$	42.82		12.18

molecular CO_2^+ cation, there are 10 possible combinations for producing the $CO_2^+ + CO_2^+$ fragmentation channel via the direct PDI process for a photon energy of 55 eV. For the dimer double-ionization potential-energy estimate, we have considered the dimer as two independent molecules. The vertical ionization potential (VIP) of the 10 states of the $CO_2^+ - CO_2^+$ system is estimated using the VIP of each isolated singly charged molecular CO_2^+ ion of the dimer, taken from Table I, while adding the Coulomb repulsion energy

between the two singly charged CO_2^+ fragments at the equilibrium distance of the dimer (6.7 a.u.). The electron energy sum is then inferred from the difference between the photon energy and the calculated VIP of the populated $CO_2^+ - CO_2^+$ states. For RCT and CT processes, we have considered the 11 lowest states of the dication in order to estimate the VIP of the $CO_2^{2+} - CO_2$ states. The two-independent-molecules model of the dimer allows us to assume a VIP($CO_2^{2+} - CO_2$) $\approx$ VIP(CO_2^{2+}). As for the direct PDI process, the electron energy sum of the RCT and CT processes is inferred from the difference between the photon energy and the calculated VIP of the $CO_2^{2+} - CO_2$ dimer dication states.

For ICD, there is no direct energy exchange between the photoelectron and the ICD electron like in the knock-off two-step-one (TS1) ionization mechanisms, for instance, meaning we can provide a kinetic-energy estimate for each of the two emitted electrons in Table III. In order to do so, treating the dimer as two independent molecules allows us to consider the VIP value for removing a single inner-valence electron from one center of the dimer, i.e., creating a $CO_2^{+*} - CO_2$ system, similar to the creation of an isolated molecular CO_2^{+*} ion as given in Table I. From the VIP($CO_2^{+*} - CO_2$) values, the photoelectron energies can be estimated for each of the eight $CO_2^{+*} - CO_2$ satellite states presented here for both photon energies used in our experiment. The estimate of the excess energy between the intermediate $CO_2^{+*} - CO_2$ dimer cation state and the final $CO_2^+ - CO_2^+$ dimer dication state at the equilibrium distance of the dimer (6.7 a.u.) is inferred from the difference of the intermediate states VIPs and the final state VIPs. The VIP values of $CO_2^+ - CO_2^+$ dimer dication states are taken from Table II. Depending on the ICD timescale, the calculated excess energy between the intermediate state and the final state can be given totally or partially to the emitted ICD electron. Assuming that ICD happens instantaneously, i.e., before a dissociation of the CO_2^{+*} site of the dimer takes place, we consider only the total transferred energy for comparing the excess energy values in Table III with the obtained experimental electron energy distributions presented in Figs. 1(c) and 1(d).

As shown in Table I, the 37.0 eV photon energy used in our experiment is below the isolated CO_2 molecule double-ionization threshold located at 37.34 eV. Since a single-

TABLE III. Molecular states of each site of the CO_2 dimer, vertical ionization potential (VIP) of ICD intermediate states at the equilibrium distance of the dimer (6.7 a.u.), photoelectron energy for photon energies of 37 and 55 eV, and available excess energy estimated from the final ionic fragment states, using the VIPs of $CO_2^+ + CO_2^+$ from Table II.

$CO_2^{+*} - CO_2$ States	VIP (eV)	Photoelectron Energy (eV)		Available Excess Energy (eV) $CO_2^+ - CO_2^+$ product states									
		$h\nu = 37$ eV	$h\nu = 55$ eV	X-X	X-A	X-B	X-C	A-A	A-B	A-C	B-B	B-C	C-C
$^2\Sigma_u^+$-$X\,^1\Pi_g$	31.9	5.1	23.1	0.28									
	33.7	3.3	21.3	2.08									
	35.3	1.7	19.7	3.68									
$^2\Sigma_g^+$-$X\,^1\Pi_g$	36.5	0.5	18.5	4.88	1.06	0.58							
	38.2		16.8	6.58	2.76	2.28	0.96						
	40.8		14.2	9.18	5.36	4.88	3.56	1.54	1.06		0.58		
	43.9		11.1	12.28	8.46	7.98	6.66	4.64	4.16	2.84	3.68	2.36	1.04
	46.1		8.9	14.48	10.66	10.18	8.86	6.84	6.36	5.04	5.88	4.54	3.24

site double-ionization process cannot be triggered below this threshold energy, it becomes clear that the two electrons must emerge from different molecular sites within the dimer. In addition, the RCT process happens at a smaller internuclear distance than the equilibrium distance of the dimer [4,24], resulting in a higher KER than the energy expected for the direct PDI and ICD mechanisms. Since the measured KER peaks at 3.8 eV for each of the photon energies used here, the RCT process can be eliminated from consideration.

For the CT process, we expect the KER to be centered at multiple values [24], depending on where the potential-energy curves of the intermediate state and the final state cross. This transition can occur in the Franck-Condon region, resulting in a KER similar to that of the direct PDI process, or at a smaller intermolecular distance as the dimer is contracting, which would result in a higher KER than the one expected for the direct PDI process. Assuming a single-electron transition takes place and using the values given in Table II, the VIP of the three states X, a, and b of the doubly ionized single site of the dimer CO_2^{2+} $[X, b,$ or $c] - CO_2$ dication amounts to 37.34, 38.52, and 39.16 eV. All these values are well above the VIP of the two-site ionized $CO_2^+[X\,^2\Pi_g] - CO_2^+[X\,^2\Pi_g]$ dimer dication, which is located at 31.62 eV. The same is true for the other single-electron transitions, where the VIPs of the intermediate states are located at least 4.66 eV above their final states. Due to this energy gap, the CT process cannot take place in the Franck-Condon region of the dimer, and consequently the CT process can be eliminated from consideration as well.

It remains to identify the contributions from the two other possible processes, direct PDI and ICD. Here we take a closer look at the measured kinetic energy of the emitted electrons in order to gather more information about the contributing electronic states of the dimer and the ionization mechanism of the process [Figs. 1(c) and 1(d)].

The electron energy distributions are displayed in Fig. 1(c) for both photon energies of 37 eV (green line) and 55 eV (black line). The latter case shows two peaks, one at low energy below 1 eV and one at high energy between 13 and 25 eV. These two separate peaks can be associated with a two-step double-ionization mechanism, wherein one electron is emitted independently from the other in each step of the process. This means that the two electrons are emitted separately with no direct energy transfer between them, which is in stark contrast to the expected uniform electron energy sharing of direct PDI and (radiative) charge transfer mechanisms and in favor of the ICD process. Furthermore, this separation in energy agrees well with the predicted electron kinetic-energy values listed in Table III for a photon energy of 55 eV. The ICD electron is expected to be in the low-energy part of the spectrum ranging between 0.28 and 14.48 eV, while the photoelectron is estimated to occupy the high-energy region of the spectrum between 8.9 and 23.1 eV. However, such a separation in kinetic energy is not expected for the PDI by a 37 eV photon, where the estimated photoelectron energy, ranging from 0.5 to 5.1 eV, and the ICD electron energy, extending from 0.28 to 4.88 eV, are actually overlapping (see Table III). This overlap is seen as a single peak in Fig. 1(c) for a photon energy of 37 eV (green line).

For a detailed investigation of the measured electron energy spectrum, we have plotted the 2D energy correlation map of the two emitted electrons as presented in Fig. 1(d). In this spectrum, we show the yield as a function of the kinetic energy of the first and the second detected electron for a photon energy of 55 eV; here the labels "first" and "second" are derived from the arrival sequence of the electrons on the detector and are physically arbitrary. In order to identify which states are involved in the decay, we have overlaid the estimated values of the correlated electron pairs on top of the experimental energy correlation map. The diagonal black full lines are associated with the different possible states of the direct PDI process, using the electron energy sum values listed in Table II. The black dots correspond to the different intermediate and final states of the ICD process, using the photoelectron and the ICD electron energy values in Table III. At a photon energy of 55 eV, two islands clearly appear in Fig. 1(d), showing a preferred unequal energy sharing between the two emitted electrons, suggesting an ICD process. By comparing the estimated electron energy correlation map with the experimental one, we see little to no contribution from the highest intermediate $CO_2^{+*} - CO_2$ state located at a VIP of 43.9 and 46.1 eV (Table III), which would produce a photoelectron kinetic energy of 8.9 and 11.1 eV and an ICD electron kinetic energy between 1.04 and 14.48 eV in Fig. 1(d). One reason for the low appearance of these two excited states is that their oscillator strength is weaker than the other six lower excited states [35]. Another reason is that higher electronic excited states lead to a faster dissociation of the CO_2^{+*} ion on the ionized dimer site, and therefore one-site dissociation of the dimer may quench the ICD process.

As mentioned in Sec. II, we also measure the monomer fragmentation channel $CO^+ + O^+$ in addition to the $CO_2^+ + CO_2^+$ dimer breakup. For a photon energy of 37.0 eV, the direct PDI of CO_2 is forbidden due to the photon energy being below the vertical double-ionization threshold of an isolated carbon-dioxide molecule at 37.34 eV. Therefore, the only possibility of creating $CO^+ + O^+$ is via autoionization, i.e., via the formation of an intermediate excited CO_2^{+*} cation that gives rise to a CO^+ ion and an autoionizing oxygen atom O^*. Taking advantage of this situation, we can compare the yields and mechanisms of the dimer breakup via ICD with the fragmentation from the autoionization channel. Unfortunately, this investigation cannot be directly correlated to a comparison between a one-site fragmentation of the dimer via autoionization with a two-site ionization of the dimer via ICD. This is because the one-site fragmentation of the dimer via autoionization is indistinguishable from the autoionization of the monomer in our experimental setup. Nevertheless, as discussed in Sec. II, due to the low concentrations of CO_2 dimers formed in the jet, the dimer ionization channel amounts to only 1.5% of the ion yield of the monomer for a photon energy of 55 eV. Therefore, the $CO^+ + O^+$ yield is dominated by ionization events from isolated carbon-dioxide monomer targets. Nevertheless, the ICD yield from all $CO_2^+ + CO_2^+$ events is found to be 14 times larger than the autoionization yield from all $CO^+ + O^+$ events. Taking into account the low dimer target density, we conclude that in dimers, the cross section for ICD is approximately 940

times larger than the cross section for autoionization. This underlines the dominance of the ICD mechanism over other ultrafast processes such as autoionization, even in a small dimer.

The low occurrence of the autoionization process in CO_2 monomers at a photon energy of 37 eV may be due to relatively small photoionization cross sections to the intermediate molecular states of the excited CO_2^{+*} cation. In carbon-dioxide monomers, the cross section of an inner-valence photoionization of CO_2 is much larger than an outer-valence ionization plus additional excitation [35]. Accordingly, the observed branching ratio between the autoionization and ICD can be traced back to the difference in ionization mechanisms, i.e., the outer-valence photoionization and excitation of CO_2 monomers and clusters (autoionization) versus the inner-valence photoionization of one site of the CO_2 dimer (ICD). Due to its long timescales, the fragmentation channel involving fluorescence, which is outrun by either ICD or autoionization, is not taken into account in our comparison.

2. $O_2^+ + O_2^+$ fragmentation channel

The KER distributions obtained for the $O_2^+ + O_2^+$ fragmentation channel are displayed in Fig. 2(a) for three photon energies, i.e., 38 eV (black line), 41.5 eV (red line), and 46 eV (green line). The distributions have similar shapes and all of them peak at a KER of 4.55 eV, which can be converted to an internuclear distance of 6 a.u. assuming a $1/R$ potential between two point charges. This is close to the most stable $|-|$ (90; 90; 0) shape geometry of the singlet state of the O_2 dimer [38], for which we would expect a KER of 4.75 eV. The O_2 dimer is a system with two open shells and this leads to asymptotically degenerate singlet, triplet, and quintet states. The singlet state has the highest binding energy [38]. For the singlet and triplet state $^{1,3}A_1$ of $O_2(X\,^3\Sigma_g^-) - O_2(X\,^3\Sigma_g^-)$, the most stable geometry is the aforementioned $|-|$ (90; 90; 0) structure with an internuclear distance of 5.77 a.u. for $^1A_1$ and 6.07 a.u. for $^3A_1$. For the quintet state $^5A_1$ of $O_2(X\,^3\Sigma_g^-) - O_2(X\,^3\Sigma_g^-)$, the most stable geometry is the X (90; 90; 90) structure with an internuclear distance of 6.22 a.u.
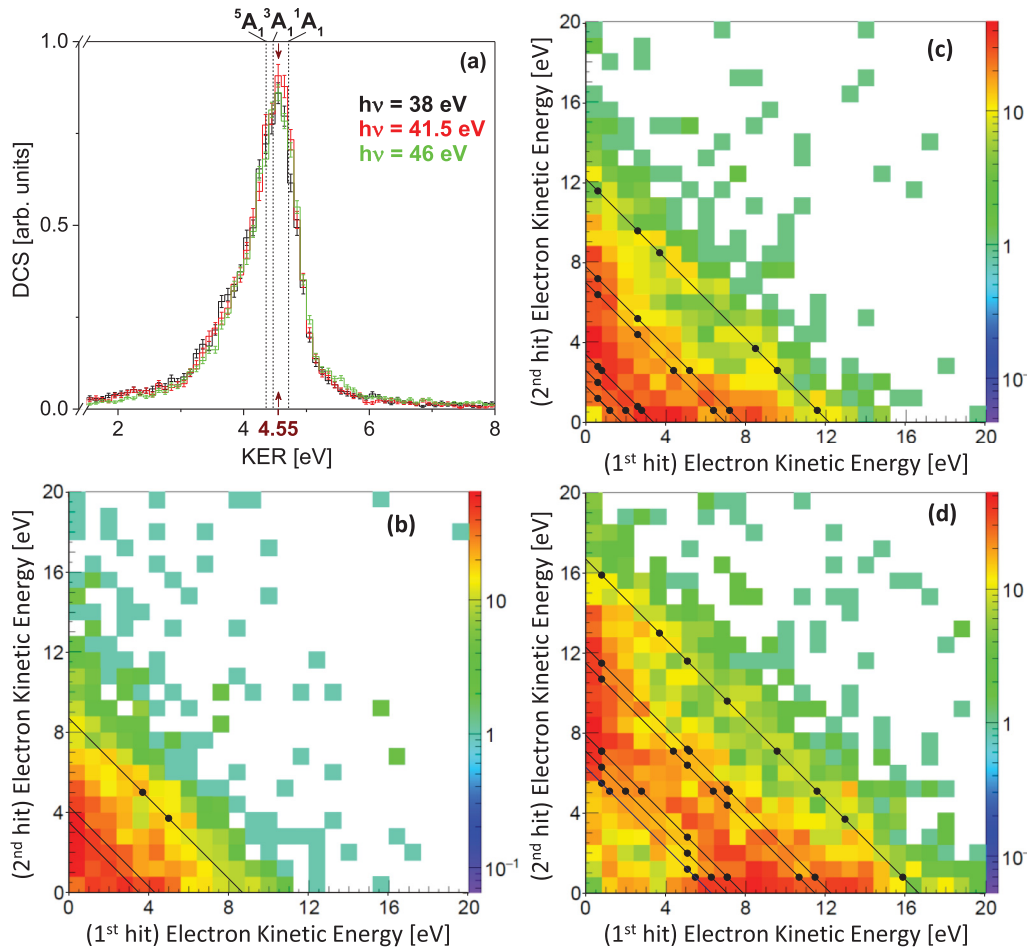

FIG. 2. (a) Differential cross section (DCS) in kinetic-energy release distributions for the $O_2^+ + O_2^+$ fragmentation channel for the PDI of O_2 dimers with photon energies of 38 eV (black line), 41.5 eV [red (dark gray) line], and 46 eV [green (gray) line], showing the same shape and a maximum located at 4.55 eV. The singlet, triplet, and quintet of $(O_2)_2$ ground states are marked as dashed lines. (b)–(d) Electron energy correlation map showing the yield of the $O_2^+ + O_2^+$ dimer breakup as a function of the energy of the first and the second detected electron for a photon energy of (b) 38 eV, (c) 41.5 eV, and (d) 46 eV. The estimated energy of the emitted electrons for direct PDI (diagonal black lines) and ICD (black dots) processes, taken from Tables V and VI, is overlaid in order to identify the implicated states and their yields. The yields in (c) and (d) are given on a logarithmic color scale.
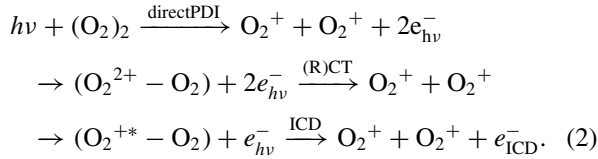
TABLE IV. Molecular states and vertical ionization potentials (VIPs) of neutral, singly, and doubly charged O_2 molecules [40,41]. Note that the electronic configuration of the O_2 molecule is $[2\sigma_g^2 2\sigma_u^2]_{IV}$ $[3\sigma_g^2 1\pi_u^4 1\pi_g^2]_{OV}$, where IV stands for inner-valence orbital and OV stands for outer-valence orbital.

Species	State	VIP (eV)
O_2	$X\,^3\Sigma_g^-$	0.0
$O_2^+{}_{OV}$	$X\,^2\Pi_g\,[1\pi_g^{-1}]$	12.3
	$a\,^4\Pi_u\,[1\pi_u^{-1}]$	16.7
	$A\,^2\Pi_u\,[1\pi_u^{-1}]$	17.5
$O_2^{+*}{}_{IV}$	$^2\Sigma_u^-\,[2\sigma_u^{-1}]$	33.0
	$^4\Sigma_g^-\,[2\sigma_g^{-1}]$	38.9
	$^2\Sigma_g^-\,[2\sigma_g^{-1}]$	40.9
	$^4\Sigma_g^-\,[2\sigma_g^{-1}]$	45.2
	$^2\Sigma_g^-\,[2\sigma_g^{-1}]$	48.4
O_2^{2+}	$X\,^1\Sigma_g^+\,[1\pi_g^{-2}]$	37.8

TABLE V. Molecular states of each site of the O_2 dimer, vertical ionization potentials (VIPs), estimated from the potential-energy curves at the equilibrium distance of the dimer (5.77 a.u.), and electron sum energies for the PDI with photon energies of 38, 41.5, and 46 eV.

States	VIP (eV)	Electron Energy Sum (eV)		
		$h\nu = 38$ eV	41.5 eV	46 eV
$O_2^+ - O_2^+$		Direct PDI	Direct PDI	Direct PDI
$X\,^2\Pi_g$-$X\,^2\Pi_g$	29.3	8.7	12.2	16.7
$X\,^2\Pi_g$-$a\,^4\Pi_u$	33.7	4.3	7.8	12.3
$X\,^2\Pi_g$-$A\,^2\Pi_u$	34.5	3.5	7.0	11.5
$a\,^4\Pi_u$-$a\,^4\Pi_u$	38.1		3.4	7.9
$a\,^4\Pi_u$-$A\,^2\Pi_u$	38.9		2.6	7.1
$A\,^2\Pi_u$-$A\,^2\Pi_u$	39.7		1.8	6.3
$O_2^{2+} - O_2$		(R)CT	(R)CT	(R)CT
$X\,^1\Sigma_g^+$-$X\,^3\Sigma_g^-$	37.8	0.2	3.7	8.2

[38]. It appears that all three states contribute to the wide KER distributions of Fig. 2(a).

The PDI of O_2 dimers results in the following conceivable reaction pathways:

$$h\nu + (O_2)_2 \xrightarrow{\text{directPDI}} O_2^+ + O_2^+ + 2e_{h\nu}^-$$

$$\rightarrow (O_2^{2+} - O_2) + 2e_{h\nu}^- \xrightarrow{\text{(R)CT}} O_2^+ + O_2^+$$

$$\rightarrow (O_2^{+*} - O_2) + e_{h\nu}^- \xrightarrow{\text{ICD}} O_2^+ + O_2^+ + e_{\text{ICD}}^-. \quad (2)$$

The most stable state of the O_2^{2+} is the $X\,^1\Sigma_g^+$ state, while the other states are highly unstable and dissociate into $O^+ + O^+$. We have considered the following final states of the O_2^+ cation: $X\,^2\Pi_g$, $a\,^4\Pi_u$, and $A\,^2\Pi_u$. Higher excited states such as $b\,^4\Sigma_g^-$, $B\,^2\Sigma_g^-$, and $c\,^4\Sigma_u^-$ predissociate in less than 100 ns into $O^+ + O$ [39]. For the assignment of possible ICD processes, we have considered the intermediate O_2^{+*} satellite states $^2\Sigma_{u,g}^-$, and $^4\Sigma_g^-$. The accessible final states and VIPs for the O_2 molecule are listed in Table IV [40,41]. The expected electron energy sum for the direct PDI and (radiative) charge transfer processes for the different dication states of the dimer are listed in Table V. The kinetic energy of the photoelectron and the ICD electron for all possible intermediate states and final states of the dimer are listed in Table VI.

This information is overlaid on the electron-electron energy correlation map, which is shown for the $O_2^+ + O_2^+$ fragmentation channel in Figs. 2(b)–2(d) for the photon energies of 38, 41.5, and 46 eV. In accordance with Tables V and VI, the estimated electron energies for the ICD process are presented as black points on the figure, while the straight black diagonal lines represent the predicted electron energy sum values for the direct PDI process.

The RCT and CT processes are expected to result in an electron energy sum of 0.2, 3.7, and 8.2 eV for photon energies of 38, 41.5, and 46 eV, respectively. These estimated electron energy sums lie under the distributions shown in Figs. 2(b)–2(d) in the form of diagonals with constant electron energy sum, but the low number of events and low resolution leads to some ambiguity in this assignment. Looking at the measured distribution shown in the electron energy correlation

map, the RCT and CT processes may play a small part in the PDI of O_2 dimers, but there must be other processes, such as direct PDI and ICD, involved in the relaxation. The electron energy correlation map in Fig. 2(d) for 46 eV shows a slight, but noticeable preference for unequal energy sharing, which is indicative of an ICD process. As shown in Table VI, the difference in energy between the photoelectrons and the ICD electrons is rather small, making an assignment difficult. Within the statistical uncertainties, the contributions from the direct PDI and ICD processes cannot be completely isolated by electron-electron energy correlations alone. In order to get more insight into the relaxation processes, we now turn to the angular distributions of the expelled electrons in the PDI process of the dimer targets.

B. Electron angular distribution in the laboratory frame

1. $CO_2^+ + CO_2^+$

To better identify the ICD contribution in the $CO_2^+ + CO_2^+$ dimer fragmentation channel, we first investigate the electron emission pattern in the laboratory frame. We have plotted the electron angular distribution with respect to the polarization axis in Fig. 3. For the dimer breakup channel at 55 eV photon energy, we have selected the relevant electrons from the electron-ion energy correlation map in Fig. 1(a). We present the polar angular distributions for high-energy electrons (13–25 eV) in Fig. 3(a) and low-energy electrons (0–7 eV) in Fig. 3(b) in order to compare the effect of the light polarization on the emission angle of the photoelectron (high energy) and the ICD electron (low energy).

With a single-photon absorption reflecting a single-particle operator, the photoelectron is emitted by linearly polarized light, and thus the emission direction of the photoelectron may hold a signature of the polarization axis. This reasoning can be applied to the emitted photoelectron initiating the ICD process, as well as to both electrons of the direct PDI and (radiative) charge transfer processes. This feature is reasonably well represented experimentally for the high-energy electron angular distribution [see Fig. 3(a)], where the photoelectron is preferentially emitted parallel to the polarization axis. The

TABLE VI. Molecular states of each site of the O_2 dimer, vertical ionization potentials (VIPs) of intermediate states of the possible ICD processes at the equilibrium distance of the dimer (5.77 a.u.), expected photoelectron energies for the PDI with photon energies of 38, 41.5, and 46 eV, and available excess energy estimated from the final ionic fragment states, using the VIPs of $O_2^+ + O_2^+$ from Table V.

		Photoelectron Energy (eV)			Available Excess Energy (eV) $O_2^+ - O_2^+$ product states					
$O_2^{+*} - O_2$ States	VIP (eV)	$h\nu = 38$ eV	$h\nu = 41.5$ eV	$h\nu = 46$ eV	X-X	X-a	X-A	a-a	a-A	A-A
$^2\Sigma_u^- \text{-} X\,^3\Sigma_g^-$	33.0	5.0	8.5	13.0	3.7					
$^4\Sigma_g^- \text{-} X\,^3\Sigma_g^-$	38.9		2.6	7.1	9.6	5.2	4.4	0.8		
$^2\Sigma_g^- \text{-} X\,^3\Sigma_g^-$	40.9		0.6	5.1	11.6	7.2	6.4	2.8	2.0	1.2
$^4\Sigma_g^- \text{-} X\,^3\Sigma_g^-$	45.2			0.8	15.9	11.5	10.7	7.1	6.3	5.5
$^2\Sigma_g^- \text{-} X\,^3\Sigma_g^-$	48.4									

angular distribution has been fitted with the anisotropy parameter β according to the well-known parametrization of the photoionization process [42,43]:

$$\frac{d\sigma}{d\Omega dE} = \frac{\sigma(E)}{4\pi}\left\{1 + \beta(E)\left[\frac{3}{2}\cos^2(\theta) - \frac{1}{2}\right]\right\}.$$

For the photoelectron [Fig. 3(a)], we found an asymmetry parameter of $\beta = 0.515 \pm 0.048$.

In an ICD process, the second electron is emitted in a separate step, i.e., the emission of the second electron happens independently from the photoionization of the first electron. Consequently, the ICD electron angular distribution is expected to be insensitive to the orientation of the polarization vector of the incoming light. The only relevant axis for the ICD electron angular distribution is the dimer axis. From the laboratory frame emission pattern of a low-energy electron (0–7 eV) in Fig. 3(b), we find an anisotropy parameter of $\beta = 0.064 \pm 0.066$, which is consistent with the isotropic emission expected from an ICD electron. This is in stark contrast to the high-energy photoelectron case (13–25 eV) presented in Fig. 3(a).

2. $O_2^+ + O_2^+$

The electron angular distributions with respect to the polarization axis for the PDI of O_2 dimers at 46 eV are presented for electrons with kinetic energies from 5 to 15 eV in Fig. 4(a) and

0 to 4 eV in Fig. 4(b). Similar to the CO_2 dimer results for a photon energy of 55 eV, the electrons with high kinetic energy between 5 and 15 eV show a preferential emission along the polarization axis with $\beta = 0.332 \pm 0.028$, while the electrons with low kinetic energy between 0 and 4 eV are emitted isotropically with respect to the polarization vector of the incoming light with $\beta = 0.002 \pm 0.017$. As discussed earlier in this section, these two plots suggest that the two electrons are emitted separately in subsequent ionization steps. This is consistent with an ICD process, where the high-energy electron is the photoelectron and the low-energy electron is the ICD electron. However, this somewhat disagrees with the values listed in Table VI and the electron energy correlation map for a photon energy of 46 eV presented in Fig. 2(d). In Table VI, we estimated an overlap of the ICD electron and the photoelectron in terms of their kinetic energies, and a clear separation could not be easily made. This suggests that the intermediate state located at VIP = 45.2 eV (see Table VI), which produces 0.8 eV photoelectrons and 5.5 to 15.9 eV ICD electrons, does not contribute to the PDI yield of the O_2 dimer, in contrast to the other listed intermediate states, which produce photoelectron energies higher than 5 eV. This may explain why the ICD electrons seem to dominate the low-energy part of the spectrum, and the photoelectron angular distribution, resembling a dipole distribution in Fig. 4(a), seems to dominate the high-energy region.
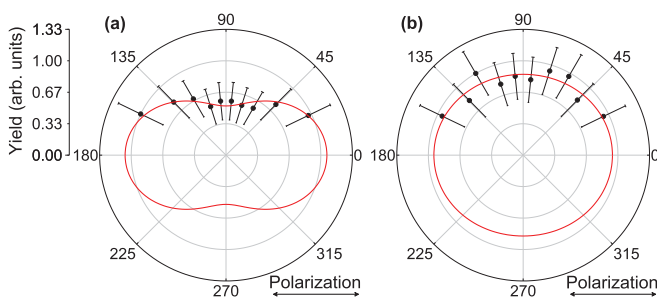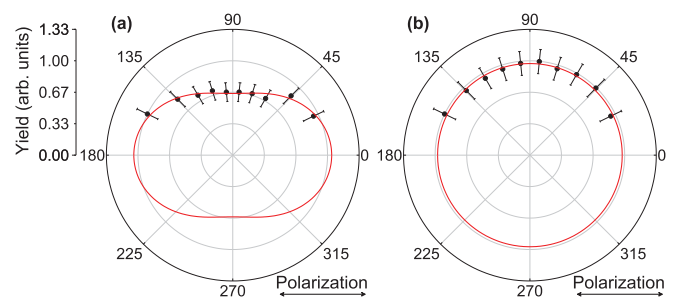

FIG. 3. Angular distribution of the (a) high-energy (13–25 eV) electron and (b) low-energy (0–7 eV) electron with respect to the polarization axis (horizontal) of the PDI of CO_2 dimers for a photon energy of 55 eV. The (red) line shows a fit $\{1 + 0.5\beta[3\cos^2(\theta) - 1]\}$ to the data points. The values of the asymmetry parameter β for (a) and (b) are equal to 0.515 ± 0.048 and 0.064 ± 0.066, respectively. All error bars represent one standard deviation in the statistical uncertainty.

FIG. 4. Angular distribution of the (a) high-energy (5–15 eV) electron and (b) low-energy (0–4 eV) electron with respect to the polarization axis (horizontal) of the PDI of O_2 dimers for a photon energy of 46 eV. The (red) line shows a fit of $\{1 + 0.5\beta[3\cos^2(\theta) - 1]\}$ to the data points. The value of the asymmetry parameter β for (a) and (b) are equal to 0.332 ± 0.028 and 0.002 ± 0.017, respectively. All error bars represent one standard deviation in the statistical uncertainty.
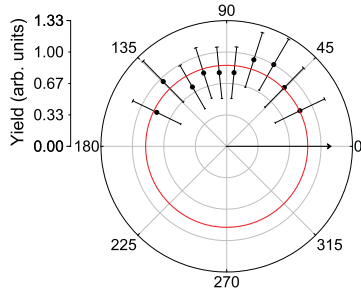
FIG. 5. Emission direction of the ICD electron, i.e., low-energy electron, with respect to the photoelectron, i.e., high-energy electron (fixed to the right as indicated by the black arrow), from the PDI of CO_2 dimers with a photon energy of 55 eV. The (red) line is a circle fitted to the data points to guide the eye. All error bars represent one standard deviation in the statistical uncertainty.

FIG. 6. Relative angle between the two emitted electrons from the PDI of O_2 dimers with a photon energy of 46 eV for (a) electrons with equal energy sharing and (b) electrons with unequal energy sharing. The higher-energy electron emission direction is fixed to the right, as indicated by the black arrows. The (red) line is a circle fitted to the data points to guide the eye. All error bars represent one standard deviation in the statistical uncertainty.

C. Relative emission angle between the two electrons

1. $CO_2^+ + CO_2^+$

The assigned ionization mechanisms are further supported by the relative emission angle between the two electrons θ_{12}, as presented in the polar plot in Fig. 5 for the PDI of CO_2 dimers at a photon energy of 55 eV. In this spectrum, the high-energy electron is always emitted to the right, as marked by the black arrow, while the relative emission angle of the low-energy electron is represented by the black dots. Because of the low count rate, we integrated over the orientation of the polarization vector of the light and the orientation of the dimer axis. Figure 5 shows that the low-energy ICD electron is emitted isotropically with respect to the photoelectron, as expected for two independently emitted electrons during the ICD process.

2. $O_2^+ + O_2^+$

In the PDI of O_2 dimers at 46 eV, shown in Fig. 6, we present the relative emission angle between two outgoing electrons for an electron energy sum between 5 and 15 eV. We have selected equal electron energy sharing by requiring an electron energy difference below 5 eV between the two measured electrons, as shown in Fig. 6(a). Unequal energy sharing in our case is defined by requiring electron energy differences higher than 5 eV; this case is shown in Fig. 6(b). Here, too, we integrate over the orientation of the dimer axis and the polarization vector of the incoming light. The relative electron-electron angular distribution, shown in Fig. 6(a), resembles a distribution with a preferred emission of the electrons into opposite hemispheres, similar to results from knock-off mechanisms, while the angular distribution, shown in Fig. 6(b), is rather isotropic, which points towards a two-step process such as ICD.

Both angular distributions are not unambiguous and both of them suffer from multihit detection problems of our electron detector, which affects the detection yield of electrons that are emitted in the same direction with similar kinetic energies and hence result in a loss of events at $\theta_{12} \approx 0^o$. The loss of such events depends on the trajectories of the electrons in our 3D momentum spectrometer, which are sensitive to the electron energy sharing E_s. For an electron energy sum of 5 to 15 eV
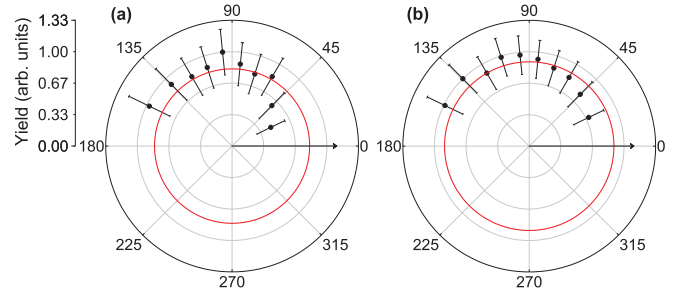
and the given spectrometer electric field, we simulated this loss to be up to 7% for equal energy sharing and about 3% for unequal energy sharing. This agrees well with the observed deviation from an isotropic molecular frame photoelectron angular distribution (MFPAD) for autoionization processes (i.e., unequal electron energy sharing) of oxygen monomers (3.5%, not shown here) in which the two emitted electrons are ionized in two separate steps, and thus the estimation of the multihit detection problems becomes possible experimentally. The measured asymmetries exhibited in Fig. 6(a) (equal electron energy sharing) are 11.2% ± 0.5% and 7.6% ± 0.4% in Fig. 6(b) (unequal electron energy sharing), which are significantly higher than the estimated multihit loss values. This suggests the presence of the knock-off process in both equal and unequal electron energy cases.

D. Electron angular distribution with respect to dimer axis

1. $CO_2^+ + CO_2^+$

We now turn to the electron emission pattern in the body-fixed frame. Again, we start our investigation by focusing on the PDI of CO_2 dimers. In Fig. 7, we show the electron angular distribution with respect to the dimer axis, which we have determined from the relative 3D momentum of the two recoil CO_2^+ ions. This represents an RFPAD since we have little to no knowledge about the orientation of the molecular CO_2^+ cations with respect to the dimer axis. Low count rates require that we integrate over the orientation of the polarization vector of the light. According to our KER measurements depicted in Fig. 1(a), we know that we mostly have the slipped parallel $/-/$ (60; 60; 0) configuration of the CO_2 dimer; however, the CO_2^+ cations may point to the left $/-/$ or to the right $\backslash-\backslash$ as well as out of the plane. As in Fig. 3, we have selected electrons from the electron-ion energy correlation map in Fig. 1(a) for a photon energy of 55 eV and the $CO_2^+ - CO_2^+$ breakup channel in order to investigate the effect of the dimer axis on the photoelectron (13–25 eV) and the ICD electron (0–7 eV) emission directions in the body-fixed frame. In our measurements, we find that the CO_2 dimer breaks up isotropically with respect to the polarization vector for both photon energies (not shown here).
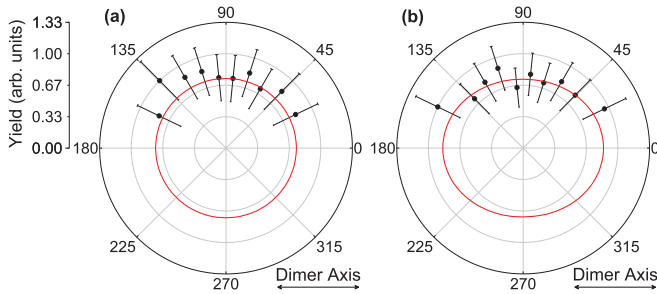
FIG. 7. Angular distribution of the (a) high-energy (13–25 eV) electron and (b) low-energy (0–7 eV) electron with respect to the dimer axis (horizontal) of the PDI of CO_2 dimers for a photon energy of 55 eV. The (red) line is a Legendre polynomial series up to fourth-order fit to the data points. All error bars represent one standard deviation in the statistical uncertainty.
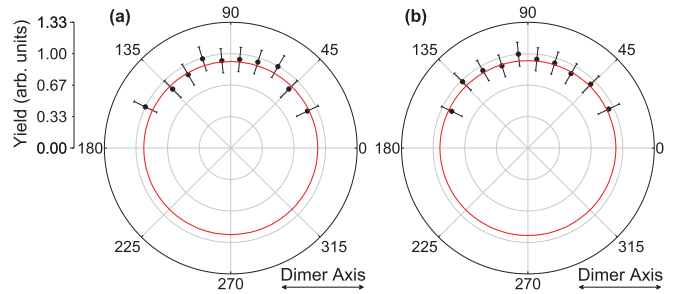

FIG. 8. Angular distribution of the (a) high-energy (5–15 eV) electron and (b) low-energy (0–4 eV) electron with respect to the dimer axis (horizontal) of the PDI of O_2 dimers for a photon energy of 46 eV. The (red) line is a Legendre polynomial series up to fourth-order fit to the data points. All error bars represent one standard deviation in the statistical uncertainty.

For a direct PDI process, we predict that the emission of the two electrons depends on the orientation of the dimer axis. This is expected because the first photoelectron is emitted in the direction of the neighboring neutral molecule of the dimer, in order to knock off another electron [25,44].

For a two-step process, we can imagine two scenarios where the decay time between the subsequent steps is fast or slow by comparison to the rotation time of the dimer axis. For slow processes such as radiative charge transfer (RCT), the fragmentation direction of the ionic breakup is irrelevant for both emitted electrons since the dimer has time to rotate between the photoionization and the fragmentation; all memory of the orientation of the dimer with respect to the polarization vector of the incoming light is washed out for both electrons in the RCT process. In contrast, for fast processes such as ICD, the fragmentation direction of the dimer may become relevant for the emitted photoelectron because the time between the photoionization step and the fragmentation step is too short to allow dimer rotation. In this case, we would expect a photoelectron angular distribution that is sensitive to the dimer recoil axis. On the other hand, it is conceivable that the emission pattern of the photoelectron can show signatures of the electronic states and orientation of the cation at one CO_2 site of the dimer. With the knowledge of the dimer structure, which in the present case is the slipped parallel $/-/$ (60; 60; 0) geometry (see KER discussion above), the photoelectron distribution in the dimer frame may show a specific emission pattern comprised of the sum of the possible molecular frame photoelectron angular distributions (MFPADs) of the two CO_2 sites (left $/-/$, right $\backslash-\backslash$, and out of the plane). If the photoelectron is instead sensitive to the dimer axis only, the emission pattern may show a less structured distribution, but likely a preferred emission along the weak bond axis. The RFPAD of the fast electron is shown in Fig. 7(a) for the PDI of CO_2 dimers with 55 eV photons. Within the statistical uncertainties, the emission patterns are consistent with an isotropic distribution or a cloverleaf shape, the latter stemming from a possible superposition of MFPADs of the CO_2 sites from the $/-/$ and $\backslash-\backslash$ geometries. There is no indication of a preferred electron emission along the dimer axis.

The low-energy (ICD) electron for the PDI of CO_2 dimers is shown in Fig. 7(b). While the ICD electron is emitted

in a second independent step and the angular distribution is isotropic in the laboratory frame, as seen in Fig. 3(b), the emission pattern in the recoil frame may in general show structure. For instance, an ICD electron originating from a valence orbital is likely not emitted isotropically since the break of the bond via ICD is sensitive to the internuclear distance between the two dimer sites. This has been observed in ICD processes of neon and helium dimers [45,46], which showed an emission pattern of the ICD electrons preferentially along the dimer axis. For the PDI of CO_2 dimers, we observe a possible subtle emission along the dimer axis in the angular distribution in Fig. 7(b); however, its statistical significance is low and the data are essentially consistent with an isotropic ICD electron emission.

2. $O_2^+ + O_2^+$

Similar considerations can be applied to the investigation of the emitted electrons from the O_2 dimer. The RFPADs for the PDI of O_2 dimers at 46 eV photon are presented in Fig. 8. We select electrons with kinetic energies of 5 to 15 eV [Fig. 8(a)] and 0 to 4 eV [Fig. 8(b)]. The electron angular distributions in the recoil frame show isotropic distributions for both electron energy ranges.

IV. SUMMARY

In this work, the competition between one-site dissociation and two-site fragmentation of carbon-dioxide dimers and oxygen dimers has been investigated via photoionization of valence electrons. The highly differential triple and quadruple coincidence experiments provide spectroscopic tools in the form of KER measurements, electron-ion and electron-electron energy correlation maps, laboratory frame angular distributions, relative electron-electron emission angles, and RFPADs to investigate the PDI of small molecular dimers in high detail. We could narrow down the relevant structures and ionization mechanisms for the molecular clusters $(CO_2)_2$ and $(O_2)_2$.

We found that the direct dissociation or autoionization of CO_2^{+*} on a single site of a CO_2 dimer is insignificant

by comparison to a fast relaxation of the dimer via ICD. The symmetric ionic breakup by ICD involving two sites of the dimer is almost a thousand times more prominent than the autoionization of one site after XUV ionization. The kinetic-energy release of the dissociating ions enabled us to pinpoint the internuclear distance at the time of fragmentation and to deduce the geometry of the dimers /−/ (60, 60, 0) by comparison with calculated intermolecular distances from the literature. We reported the kinetic-energy range of the emitted photoelectrons and the ICD electrons and compared them to estimates based on the well-known monomer states. This enabled us to coarsely identify the contributing electronic states in the ICD process.

For the investigation of the PDI of O_2 dimers, we applied the same approach. The KER measurements revealed a preferred |−| (90, 90, 0) structure of the dimer. The electron angular distributions with respect to the polarization axis looked very similar to the PDI of CO_2 dimers. In both cases, we see a signature of a two-step process, emitting a photoelectron preferentially along the polarization direction and an isotropically emitted ICD electron. However, for the PDI of O_2 dimers, the electron-electron energy correlation map and the relative emission angle between the two electrons showed contributions from ICD as well as direct PDI (knock-off) processes. Furthermore, the RFPADs integrated over the polarization direction of the incoming light did not separate these two processes. Therefore, the question remains open of why the PDI of O_2 dimers shows a contribution from knock-off processes and the PDI of CO_2 dimers does not.

Investigation of the PDI of O_2 dimers at higher photon energies in the future is expected to be fruitful. This would help to better identify the ICD process and to separate the ICD electron from the emitted photoelectron and hence distinguish it from the knock-off mechanism. Moreover, we would learn which contributions prevail and are more important in terms of radiation damage. Further investigations with different photon energies and higher-energy resolution should help us to precisely identify the intermediate and final states. Such a state-resolved measurement may allow one to extract the ICD rates of each transition between the intermediate and final states using a similar method as in Ref. [47] and to study any effect involving the symmetries of the occupied orbitals on the ICD rates. In the near future, the same ICD identification methodology could also be employed in the investigation of the dissociation dynamics involving larger molecular clusters.

[1] T. Jahnke *et al.*, Phys. Rev. Lett. **93**, 163401 (2004).

[2] E. F. Aziz *et al.*, Nature (London) **455**, 89 (2008).

[3] H.-K. Kim, H. Gassert, M. S. Schöffler, J. N. Titze, M. Waitz, J. Voigtsberger, F. Trinter, J. Becht, A. Kalinin, N. Neumann *et al.*, Phys. Rev. A **88**, 042707 (2013).

[4] W. Iskandar *et al.*, Phys. Rev. Lett. **114**, 033201 (2015).

[5] S. Yan *et al.*, Phys. Rev. A **88**, 042712 (2013).

[6] X. Ren *et al.*, Nat. Commun. **7**, 11093 (2016).

[7] U. Hergenhahn, J. Electron Spectrosc. Relat. Phenom. **184**, 78 (2011).

[8] T. Jahnke, J. Phys. B **48**, 082001 (2015).

[9] L. S. Cederbaum, J. Zobeley, and F. Tarantelli, Phys. Rev. Lett. **79**, 4778 (1997).

[10] I. B. Muller and L. S. Cederbaum, J. Chem. Phys. **125**, 204305 (2006).

[11] R. Santra, J. Zobeley, L. S. Cederbaum, and N. Moiseyev, Phys. Rev. Lett. **85**, 4490 (2000).

[12] S. Marburger, O. Kugeler, U. Hergenhahn, and T. Möller, Phys. Rev. Lett. **90**, 203401 (2003).

[13] G. Öhrwall *et al.*, Phys. Rev. Lett. **93**, 173401 (2004).

[14] Y. Morishita *et al.*, Phys. Rev. Lett. **96**, 243402 (2006).

[15] P. Lablanquie *et al.*, J. Phys. Chem. **127**, 154323 (2007).

[16] T. Havermeier, T. Jahnke, K. Kreidi, R. Wallauer, S. Voss, M. Schöffler, S. Schössler, L. Foucar, N. Neumann, J. Titze *et al.*, Phys. Rev. Lett. **104**, 133401 (2010).

[17] T. Ouchi *et al.*, Phys. Rev. A **83**, 053415 (2011).

[18] F. Trinter *et al.*, Nature (London) **505**, 664 (2013).

[19] T. Jahnke *et al.*, Nat. Phys. **6**, 139 (2010).

[20] M. Mucke *et al.*, Nat. Phys. **6**, 143 (2010).

[21] U. Hergenhahn, Int. J. Radiat. Biol. **88**, 871 (2012).

[22] E. Alizadeh, T. M. Orlando, and L. Sanche, Annu. Rev. Phys. Chem. **66**, 379 (2015).

[23] P. H. P. Harbach *et al.*, J. Phys. Chem. Lett. **4**, 943 (2013).

[24] K. Kreidi, T. Jahnke, T. Weber, T. Havermeier, X. Liu, Y. Morisita, S. Schossler, L. P. H. Schmidt, M. Schoffler, M. Odenweller *et al.*, Phys. Rev. A **78**, 043422 (2008).

[25] T. Havermeier, T. Jahnke, K. Kreidi, R. Wallauer, S. Voss, M. Schöffler, S. Schössler, L. Foucar, N. Neumann, J. Titze *et al.*, Phys. Rev. Lett. **104**, 153401 (2010).

[26] R. Dörner *et al.*, Phys. Rep. **330**, 95 (2000).

[27] J. Ullrich *et al.*, Rep. Prog. Phys. **66**, 1463 (2003).

[28] T. Jahnke *et al.*, J. Electron Spectrosc. Relat. Phenom. **141**, 229 (2004).

[29] A. Zulfiqar *et al.*, Proc. SPIE **8502**, 85020P (2012).

[30] R. Dörner *et al.*, *Imaging in Chemical Dynamics* (ACS Symposium Series), edited by A. G. Suits and R. E. Continetti (Oxford University Press, Oxford, 2000), pp. 339–349.

[31] O. Jagutzki *et al.*, IEEE Trans. Nucl. Sci. **49**, 2477 (2002).

[32] R. N. Zare, J. Chem. Phys. **47**, 204 (1967).

[33] R. N. Zare, Mol. Photochem. **4**, 1 (1972).

[34] Y. N. Kalugina *et al.*, J. Chem. Phys. **140**, 234310 (2014).

[35] Q. Tian *et al.*, J. Chem. Phys. **136**, 094306 (2012).

[36] P. Millie *et al.*, J. Chem. Phys. **84**, 1259 (1986).

[37] A. E. Slattery *et al.*, J. Chem. Phys. **122**, 084317 (2005).

[38] M. Bartolomei *et al.*, Phys. Chem. Chem. Phys. **10**, 5374 (2008).

[39] F. B. Yousif *et al.*, J. Phys. B **20**, 5079 (1987).

[40] J. Rolke *et al.*, Chem. Phys. **230**, 153 (1998).

[41] M. Larsson *et al.*, J. Phys. B **23**, 1175 (1990).

[42] G. H. Dunn and L. J. Kieffer, Phys. Rev. **132**, 2109 (1963).

[43] R. N. Zare and D. R. Herschbach, Proc. IEEE **51**, 173 (1963).

[44] H. Ni, C. Ruiz, R. Dörner, and A. Becker, Phys. Rev. A **88**, 013407 (2013).

[45] T. Havermeier, K. Kreidi, R. Wallauer, S. Voss, M. Schöffler, S. Schössler, L. Foucar, N. Neumann, J. Titze, H. Sann *et al.*, Phys. Rev. A **82**, 063405 (2010).

[46] T. Jahnke *et al.*, J. Phys. B **40**, 2597 (2007).

[47] J. Rist *et al.*, Chem. Phys. **482**, 185 (2017).